Electrokinetic transport regulation at liquid-infused surface by liquid depletion and ion partition

Yunfan Huang and Moran Wang*
Department of Engineering Mechanics and SKL of ASP, Tsinghua University, Beijing 100084, China

(Received 17 March 2025; accepted 20 May 2026; published 18 June 2026)

The interest in spontaneous charging and electrokinetic transport at immiscible liquid-liquid interfaces originated from early studies on biological membrane functions and elementary charge measurements. In recent years, with the rapid advancement of micro- and nanofabrication and measurement technologies, the regulation of multiphase flow and transport at micro- and nanoscales based on electrokinetic transport at liquid-liquid interfaces has become feasible. Among these, slippery liquid-infused surfaces (SLIS) have garnered significant attention, while several practical issues and potential mechanisms of electrokinetic transport regulation with SLIS remain unclear. This paper employs direct numerical simulations based on the diffuse interface model to explore the impact of groove oil depletion effects on electroosmosis and the influence of two-sided ion partition effects on streaming potential at SLIS. The study reveals the electroosmotic velocity reversal effect induced by geometric configurations, as well as the two-sided streaming potential effect induced by mixing and partitioning-induced charging. These findings provide foundational insights for the rational design of quantitative electrokinetic regulation strategies for multiphase flow at micro- and nanoscales.

DOI: 10.1103/6nkj-19qw

I. INTRODUCTION

Due to interfacial specific adsorption or interphase imbalanced partition of ions [1–4], liquid-liquid interfaces can get spontaneously charged, leading to electrokinetic transport under nonequilibrium potential differences [5–7]. This is of significant importance since it provides a novel approach for the active control of multiphase flow and transport at micro- and nanoscales [8–12], Due to the fluidity of liquid-liquid interfaces, recent studies have explored their electrokinetic transport in typical scenarios such as enhancing two-phase displacement, micro- and nanoscale liquid pumping, and mechanical energy conversion and harvesting [13–21]. In two-liquid electroosmosis and streaming potential systems, the geometric configurations are typically low-dimensional parallel shear flows within quasi-two-dimensional microchannels. As the length of the liquid-liquid interface increases, interfacial disturbances may gradually amplify, potentially leading to various interfacial flow instability issues [22–24]. Therefore, in practical applications, systems with special geometric constraints are often employed to stabilize the liquid-liquid interface. Representative examples include droplets in three-dimensional microchannels and surfaces with periodic microstructures [25]. Slippery liquid-infused surface (SLIS) is a typical type of heterogeneous surface, composed of periodically arranged liquid-filled grooves, which can be considered as a liquid version of superhydrophobic surfaces to some extent [26], and are widely found in nature and engineering applications, exhibiting excellent properties similar to superhydrophobic surfaces, such as self-cleaning, anti-icing, wettability control, and surface drag reduction [27]. In this work, we will

*Contact author: mrwang@tsinghua.edu.cn

focus on the practical issues and potential mechanisms of electrokinetic transport regulation with SLIS.

On the one hand, since the effective slip effect of hydrophobic surfaces was discovered, due to the similar magnitude between the slip length and the Debye length, the electroosmotic slip velocity on such surfaces may be amplified [28]. The electroosmosis enhancement effect by surface velocity slip at superhydrophobic surface and SLIS has been extensively studied by previous researchers [29]. Squires was one of the first to notice the electrokinetic flow phenomena that could arise from inhomogeneous slip interfaces. Based on the thin electric double layer assumption, the relationship between the effective electroosmotic slip velocity and the interfacial charge, roughness, and Debye length is established, with discussions on the potential applications of electroosmotic pumps through flow rate relationships [30]. Typically, it is assumed that the liquid-liquid interface remains flat with the solid-liquid interface during transport, allowing the relationship between slip velocity and the effective slip length of the liquid-liquid interface to be asymptotically derived in a straightforward way using linear dissipation theory and the principle of energy reciprocity. Subsequently, scholars have conducted detailed studies on factors such as groove anisotropy and the type of infused liquid [31,32]. However, research has shown that interfacial shear can lead to the depletion of liquid within the grooves (i.e., the depletion effect) [33], which may result in the failure of slip performance in SLIS [34]. This groove oil depletion effect may impact the electroosmotic slip behavior of liquid-infused surfaces, which is of significant importance for practical applications such as micro- and nanoscale liquid pumping, while there is still lacking of studies yet addressing this issue.

On the other hand, considering that the streaming potential arises from the convective current generated by a pressure gradient, SLIS are highly advantageous for enhancing energy conversion by increasing the streaming potential. Extensive research has been conducted on the streaming potential effect in the main channel of SLIS, but these studies have been limited to inert hydrophobic systems with single-sided adsorption-induced interface charging at two-liquid interface [35–37]. For systems composed of polar oils and organic ions, such as ITIES (interface between two immiscible electrolyte solutions), a few studies have discussed the streaming potential effect within the grooves. Pascall and Squires once treated SLIS as a simplified case of droplet electrophoresis, investigating the electroosmotic mechanism of surfaces infused with conductive dielectric liquids [5]. Based on the assumptions of a very weak external electric field and linear superposition, their study systematically discussed the electrokinetic slip effects of grooves infused with liquids of different conductive and dielectric properties, focusing on the influence of surface conductivity on the electroosmotic flow of two-phase liquids. The study pointed out that the slip characteristics of the liquid-liquid interface can enhance the electroosmotic velocity, and when the interfacial charge is large, a significant surface conductivity effect can also be observed, which suppresses the electroosmotic flow. A key assumption in this study is that the conductive dielectric liquid within the grooves maintains electrochemical equilibrium in the normal direction. Under this condition, the tangential electric field acting on ions in the electric double layer at the liquid-liquid interface balances the tangential osmotic pressure gradient caused by inhomogeneous charging, resulting in a zero electric field in the bulk neutral region of the liquid within the grooves. However, for the double-sided diffuse layers, under tangential nonequilibrium transport conditions, ions in the electric double layer inside the grooves may also accumulate downstream, potentially inducing a nonzero streaming potential within the grooves. This would cause the bulk region of the liquid in the grooves to exhibit a nonzero reverse electric field. Inspired by this, for SLIS with conductive dielectric liquids, when a pressure gradient exists between the upstream and downstream of the main channel, the coupling of two-sided charging polarization due to ion partitioning effects may also lead to a streaming potential effect within the grooves, which could be more easily collected in series.

The diffuse interface model employs a continuous distribution of properties and physical fields across the interface. This allows for the bottom-up incorporation of interactions between solute ions and the fluid background of solvent molecules by associating interfacial physicochemical properties with solvent phase fractions [38]. This approach is essential for resolving the complex charging

mechanisms and nonequilibrium transport features, and this paper will adopt the diffuse interface model to explore the electrokinetic transport behaviors of SLIS with infused dielectric liquid which may be conductive. In fact, for those liquid-liquid interfaces that may exhibit partition-induced charging, the sharp interface model often struggles to capture the effects of solvent mixing at the liquid-liquid interface on complex partitioning, adsorption charging, and shear stress matching relationships. Additionally, it is usually hard to describe the intricate kinetic behaviors of ion transport along and across the mobile interface [7]. Besides, while matched asymptotic expansions based on the sharp interface models can provide effective boundary conditions under specific small-parameter limits, they are generally inadequate for capturing interfacial nonequilibrium transport behaviors under broader conditions [39].

For those exhibits nonlinear characteristics, with the system geometry typically lacking of high-order symmetry, the precise solutions often rely on direct numerical simulations, and our previous work presents a promising solution [7]. However, for strongly nonequilibrium electrokinetic transport scenarios involving interfacial-induced charging and significant tangential concentration polarization (such as droplet electrophoresis, two-phase streaming potential, and electrokinetics of SLIS), the aforementioned work using a regular perturbation solution based on the modified Poisson-Boltzmann equation, which strongly relies on the assumption of electrochemical quasiequilibrium, becomes inadequate. In fact, for ITIES systems composed of polar oils and organic ions, the distribution potential is uniform under thermodynamic equilibrium. However, under nonequilibrium transport conditions with tangential nonequilibrium potential fields at the interface, the convective behavior of the liquid-liquid interface on SLIS and the nonzero tangential mobility of ions will lead to their accumulation downstream, potentially resulting in inhomogeneous charging. This may induce inhomogeneous interfacial charge or distribution potentials, and even cause ions in the diffuse layer to exhibit nonuniform transport, inducing normal currents. These effects, in turn, will influence the interfacial nonequilibrium electrokinetic flow behavior.

This paper focuses on the typical electrokinetic transport behaviors of liquid-infused slippery surface systems, demonstrating the application potential of electrokinetic transport in achieving the active and rational control of micro- and nanoscale multiphase flow and transport. In particular, this is the first work offering a direct numerical simulation to those two-liquid electrokinetics with complex symmetry-breaking geometry and strong nonequilibrium transport. This work also highlights the significance of the previously developed diffuse interface model for conducting quantitative research on the mechanisms of electrokinetic transport at liquid-liquid interfaces. Due to the high computational cost associated with the relevant systems, this preliminary study primarily employs qualitative and semi-quantitative case analysis methods. Specifically, Sec. II introduces the diffuse interface model and the solution methods; Secs. III and IV investigate the effects of groove liquid depletion on interfacial electroosmosis and the coupling effects of two-sided charging polarization on interfacial streaming potential; and Sec. V presents the conclusions. The verification of the feasibility of direct numerical simulations is given in the Appendix.

II. MODELS AND METHODS

Here we utilize the diffuse interface model developed in the previous work to describe the electrokinetic transport of two-liquid interface [7], which is briefly summarized below.

The evolution of phase order parameter obeys the Cahn-Hilliard equation

$$\frac{\partial \phi}{\partial t} + \boldsymbol{u} \cdot \nabla \phi = \nabla \cdot (M \nabla \mu_\phi), \tag{1}$$

where ϕ is the order paramter, $\boldsymbol{u}$ is the local fluid velocity, $M = \chi(\phi)\varepsilon_{\rm pf}^2$ is the mobility parameter, and $\mu_\phi = \Lambda[-\nabla^2\phi + (\phi^2 - 1)\phi/\varepsilon_{\rm pf}^2]$ is the chemical potential of the solvent mixture. The interface tension coefficient is linked to the phase field parameter $\varepsilon_{\rm pf}$ by $\gamma = (2\sqrt{2}/3)\Lambda/\varepsilon_{\rm pf}$. The no flux

condition for μ_ϕ at solid wall is utilized [40], i.e., $\nabla_n \mu_\phi = 0$, and the contact angle θ is imposed in a geometric manner [41,42], i.e., $\nabla_n \phi = |\nabla \phi| \cos\theta$.

The Navier-Stokes equations are utilized for the incompressible fluid flow

$$\begin{aligned} \nabla \cdot \boldsymbol{u} &= 0, \\ \bar{\rho} \frac{\partial \boldsymbol{u}}{\partial t} + \bar{\rho} \boldsymbol{u} \cdot \nabla \boldsymbol{u} &= -\nabla p + \nabla \cdot (\bar{\mu} \nabla \boldsymbol{u}) + \boldsymbol{F}_{\mathrm{st}} + \boldsymbol{F}_{\mathrm{e}}. \end{aligned} \tag{2}$$

Here, $\boldsymbol{u}$, p are the fluid velocity and pressure, respectively, $\boldsymbol{F}_{\mathrm{st}} = \mu_\phi \nabla \phi$ the continuous form of interface tension force, and $\boldsymbol{F}_{\mathrm{e}} = \rho_e \boldsymbol{E} - (1/2) E^2 \nabla \bar{\varepsilon}$ the electromechanical force derived from the Maxwell stress, in which $\boldsymbol{E} = -\nabla \varphi$ is the overall electric field. No-slip boundaries are utilized for fluid flow, while the moving contact line can be triggerd through the phase diffusion [40].

The Poisson equation for the electric potential φ is written as

$$-\nabla \cdot (\bar{\varepsilon} \nabla \varphi) = \rho_e. \tag{3}$$

For the boundary condition at solid wall $\Gamma_{\mathrm{ls}}^{(\alpha)}$ in contact with liquid phase α, the constant surface charge density condition is used

$$\boldsymbol{n} \cdot \varepsilon_\alpha \nabla \varphi|_{y \in \Gamma_{\mathrm{ls}}^{(\alpha)}} = -\sigma_{\mathrm{ls}}^{(\alpha)}, \tag{4}$$

where $\boldsymbol{n}$ is the normal vector at the solid wall pointing into the solution. Note that here we have neglected the electrical polarization inside the solid region.

Ion transport is described by the *modified* Nernst-Planck equation

$$\frac{\partial n_i}{\partial t} + \nabla \cdot \boldsymbol{j}_i^{**} = 0, \tag{5}$$

where n_i is the number density of ion i. Here, the ionic flux of ion i is given by

$$\boldsymbol{j}_i^{**} = n_i \boldsymbol{u} - \bar{D}_i \left(\nabla n_i + n_i \nabla \ln \gamma_i^\phi \right) - \frac{z_i e \bar{D}_i}{k_{\mathrm{B}} T} n_i \nabla \varphi, \tag{6}$$

in which the additional free energy term $\Delta g_i(\phi) \equiv \Delta g_i^{(\mathrm{t})}(\phi) + \Delta g_i^{(\mathrm{a})}(\phi)$ has been added into the original Nernst-Planck equation,

$$\gamma_i^\phi := \exp\left(\frac{\Delta g_i(\phi)}{k_{\mathrm{B}} T} \right). \tag{7}$$

Note that those additional free energies can be determined by the prescribed surface charge density and/or distribution potentials at the two-liquid interface [7]. The no flux condition $\boldsymbol{j}_i^{**} \cdot \boldsymbol{n} = 0$ is utilized at the solid wall, while $n_{i,\alpha} = n_{i,\alpha}^\infty$ is imposed at the far field within the bulk region of phase α.

Concerning the material properties, $\bar{\rho}$, $\bar{\mu}$, $\bar{\varepsilon}$, and $\bar{D}_i$ are the local phase interpolations of fluid density, dynamic viscosity, permittivity, and ionic diffusivity, respectively. In this work, the material properties are assumed to have the linear dependence on the volume fraction ϕ_α of phase α as default ($\alpha = \mathrm{w}, \mathrm{o}$), i.e., $\bar{X} \equiv X(\phi) = \sum_\alpha X_\alpha \phi_\alpha$, where $X = \rho, \mu, \varepsilon, D_i$. For sake of simplicity, the material ratios between the oil and aqueous phases are taken as $\eta_r = \rho_r = \varepsilon_r = 1$, and the salt of 1:1 type is used. The ionic diffusivities in the aqueous phase take the same properties as KCl, while those in the oil phase are determined by the Stokes-Einstein relation [7]. In this work, the interface thickness parameter $\varepsilon_{\mathrm{pf}}$ takes the value of 0.5 nm, which is a physically reasonable value [43] and much thinner than the Debye length (10 nm) in this study. If the Debye length becomes smaller for those concentrated solutions, then the sensitivity of the interface thickness should be justified, which will not be covered in this work. The phase mobility is chosen as $\chi(\phi) \equiv \chi_0 = 10\,\mathrm{m\,s/kg}$, which is not sensitive to the final steady state of the electrokinetic transport, but only affects the evolution timescale of the phase field [40]. The interfacial tension is fixed at $\gamma = 0.05\,\mathrm{N/m}$ which is taken

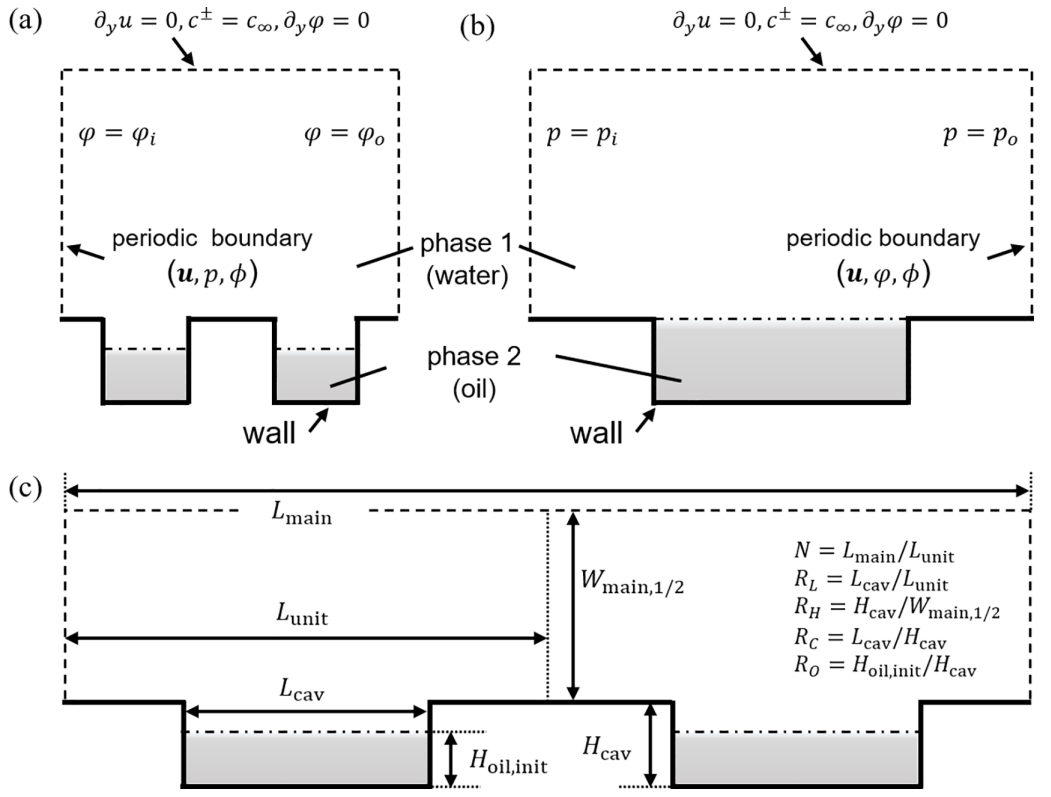

FIG. 1. Two typical setups of electrokinetic transport at liquid-infused surface. (a) Electroosmosis with possible liquid depletion. (b) Streaming potential with possible ion partition. (c) Definitions of geometrical dimensions of the system, as well as the corresponding dimensionless numbers.

as the corresponding property of oil-water interface and used to maintain the interface shape, while the contact angle is $\theta = \pi/2$ without loss of generality.

The schematics of the liquid-infused surface to be studied in this work is shown in Fig. 1. Periodic flow conditions for $\boldsymbol{u}, \phi$ are applied at the inlet and outlet boundaries, i.e.,

$$\boldsymbol{u}_{\text{in}} = \boldsymbol{u}_{\text{out}}, \ \phi_{\text{in}} = \phi_{\text{out}}, \tag{8}$$

while the pressure and electric potential are set as

$$p_{\text{in}} - p_{\text{out}} = \Delta p, \ \varphi_{\text{in}} - \varphi_{\text{out}} = \Delta\varphi \tag{9}$$

to drive the electrokinetic transport in different setups of electroosmosis and streaming potential. The upper boundary is chosen to be symmetric for u, c, and φ. As for the geometric setup, the half-width and length of the main channel are denoted by $W_{\text{main},1/2}$ and $L_{\text{main}} = N_{\text{unit}} L_{\text{unit}}$, respectively, the depth and length of the liquid-infused groove denoted by H_{cav} and L_{cav}, respectively, and the oil phase height of the groove denoted by $H_{\text{oil,init}}$, as shown in Fig. 1. To define the geometric structure of the groove and main channel, four additional ratios can be defined as $R_L \equiv L_{\text{cav}}/L_{\text{unit}}$, $R_H \equiv H_{\text{cav}}/W_{\text{main},1/2}$, $R_C \equiv L_{\text{cav}}/H_{\text{cav}}$, and $R_O \equiv H_{\text{oil,init}}/H_{\text{cav}}$. The finite element method is used to directly solve the above original problem in the simulation of two-liquid streaming potential, while the simplified version using the linearized perturbation equations with local electrochemical equilibrium and geometry-modulated electric field is adopted in the simulation of two-liquid electroosmosis considering the relatively weak nonequilibrium within it. The detailed treatment

of the numerical solver as well as the applicability of the above physical model can be found in the previous work [7].

In the next two sections, we will analyze the typical mechanisms of electrokinetic regulation on SLIS, which will focus on the impact of the groove liquid depletion effect on electroosmosis and the influence of two-sided ion partition effects on streaming potential. It should be noted that since the surface charge density of two-liquid interface is often *a posteriori*, it is hard to present a straightforward validation through comparison between theory and experiment in the liquid-infused scenarios. Nevertheless, we have verified the simulation method based on the mPB equation through comparison with the solution of the mPNP equations, as given in the Appendix. For simple systems, we have given the related verifications and validations in our previous work [7].

III. LIQUID DEPLETION EFFECT ON ELECTROOSMOSIS

To investigate the influence of the liquid depletion effect in grooves on the electroosmotic slip behavior of SLIS, this study adopts the system configuration shown in Fig. 1(a). The width-related geometric dimensions are set to $W_{\text{main},1/2} = 1\,\mu\text{m}$ with $R_H = 0.1$, the initial oil height $R_O = 1.0,\ 0.8,\ 0.6,\ 0.4,\ 0.2$, corresponding to depletion ratios $R_D = 0,\ 0.2,\ 0.4,\ 0.6,\ 0.8$, respectively. Periodic boundary conditions are applied to the velocity and pressure at the inlet and outlet boundaries, with an applied electric field strength of $E_\infty = 10^5$ V/m, resulting in $\varphi_{\text{out}} - \varphi_{\text{in}} = E_\infty L$. An aqueous electrolyte solution with a concentration of 1 mM is used, and the slip length at the solid-liquid interface is set to 0.1 nm [28]. The reference surface charge density is defined as $\sigma_0 = -2\ \text{mC/m}^2$. The total simulation time is 1×10^{-5} s, by which the system has reached a steady state.

A. Phenomena: Electroosmotic velocity reversal

To illustrate the phenomena, the length-related geometric dimensionless parameters here are set to $R_C = 1$ and $R_L = 0.5$, with $N = 2$ to satisfy the stress-free condition at infinity while keeping the computational load within an acceptable range. The liquid-liquid interface is assumed to be adsorption-charged and negatively charged of $\sigma_{\text{ll}} = \sigma_0$, which means that there only exists a single-sided diffuse layer. Results indicate that the selection of parameters such as the sub-nanometer slip length and the perturbative external electric field strength has no significant impact on the qualitative results. The electroosmotic slip velocities for grooves vary with varying degrees of polar oil depletion, qualitatively shown in the velocity field and dimensionless magnitude contour plots in Fig. 2.

Specifically, when the solid wall is uncharged (i.e., $\sigma_{\text{sl}} = 0$), as depicted in Fig. 2(a), the electroosmotic slip region in the main channel is entirely induced by the electroosmotic flow of the charged liquid-liquid interface. The electroosmotic slip velocity is opposite to the direction of the electric field in the absence of depletion, as the diffuse layer of the liquid-liquid interface is negatively charged. As the depletion effect gradually increases, the electroosmotic slip velocity transitions from opposing to aligning with the electric field direction. In this case, as the depletion effect intensifies, the geometric constraint imposed by the groove on the liquid-liquid interface flow gradually strengthens, eventually forming a distinct vortex at the junction between the groove and the main channel. This evolution of the vorticity influence range, driven by the interface configuration and geometric constraints, is likely a key reason for the reversal of the velocity direction in the main channel outside the groove compared to the electroosmotic flow direction immediately above the liquid-liquid interface within the groove.

However, if the solid-liquid interface carries the same charge density as the liquid-liquid interface (i.e., $\sigma_{\text{sl}} = \sigma_{\text{ll}}$), as shown in Fig. 2(b), the electroosmotic slip velocity always aligns with the direction induced by the solid-liquid interface, with its minimum value occurring at a depletion ratio of 0.6. Although the electroosmotic slip velocity in the main channel region consistently aligns with the electroosmotic direction of the solid-liquid interface, the significantly enhanced shear

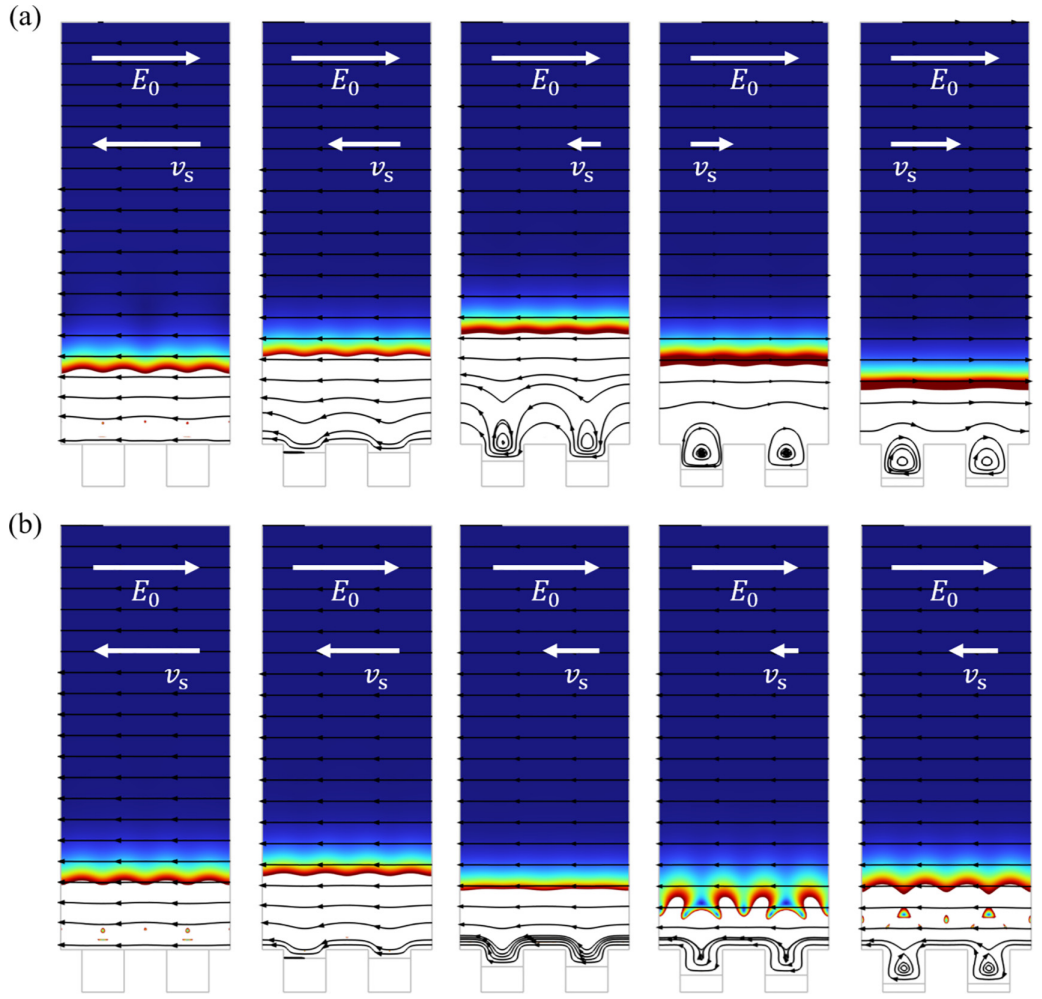

FIG. 2. Comparison of the dimensionless velocity field results for electroosmosis on SLIS: (a) The solid-liquid interface is uncharged, i.e., $\sigma_{sl} = 0$; (b) The solid-liquid interface carries the same charge as the liquid-liquid interface, i.e., $\sigma_{sl} = \sigma_{ll}$. From left to right, the depletion ratios of the oil phase in the groove are 0, 0.2, 0.4, 0.6, and 0.8, respectively. The liquid-liquid interface is assumed to be adsorption-charged and always positively charged. The color represents the relative magnitude of the velocity compared to the stress-free region (i.e., the electroosmotic slip velocity v_s), with blue regions indicating a ratio of 1 and white regions indicating values below a given cutoff threshold.

near the groove at a depletion ratio of 0.6 leads to faster velocity dissipation, thereby reducing the electroosmotic slip velocity in the main region.

B. Physicochemical effect: Adsorption versus partition

Here we compare the electroosmotic slip velocities induced by adsorption charging and partitioning charging at the liquid-liquid interface under varying depletion ratios, where the length-related geometric dimensionless parameters here are kept at $R_C = 1$ and $R_L = 0.5$, with $N = 2$. The partition-induced case corresponds to $\Delta\varphi = \varphi_T \equiv -k_B T/e$, while the adsorption-induced corresponds to a constant surface charge density of $\sigma_{ll} = \sigma_0$. The results are shown in Fig. 3.

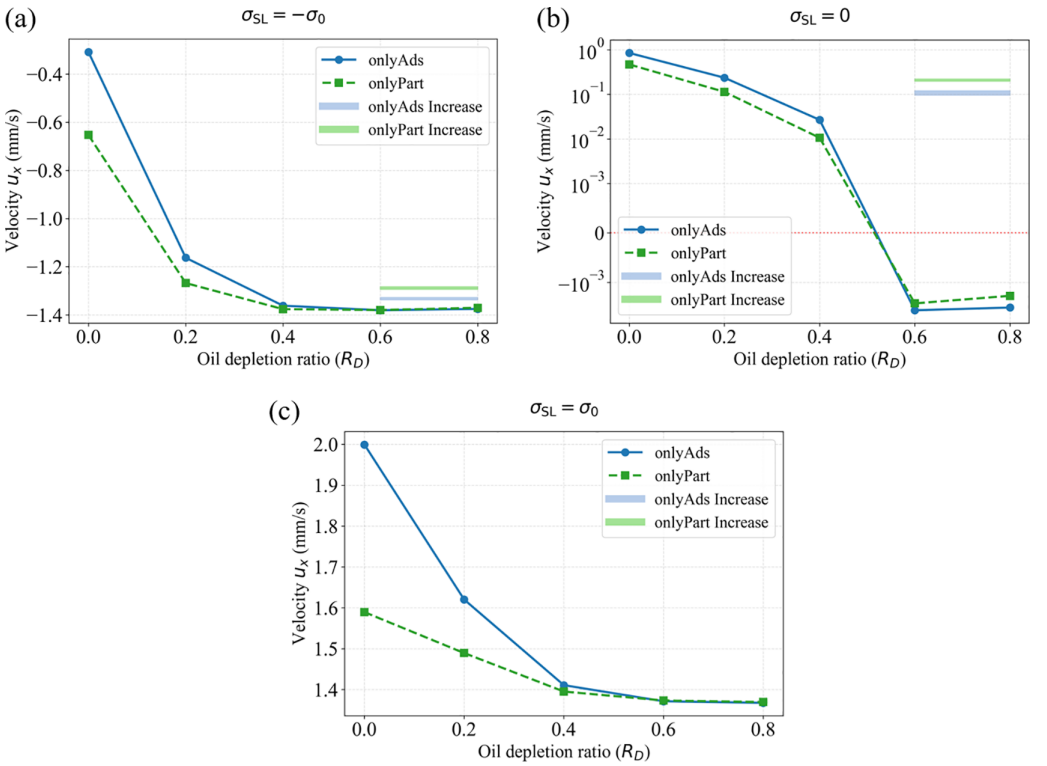

FIG. 3. The electroosmotic velocity versus oil depletion ratio for adsorption charging and partitioning charging at the liquid-liquid interface. The liquid-liquid interface chargings are set to σ_{ll}, effectively, while the solid-liquid interface charge has different conditions, including (a) $\sigma_{sl} = -\sigma_0$; (b) $\sigma_{sl} = 0$; (c) $\sigma_{sl} = \sigma_0$. Note that the colored blocks denote the oil depletion ratio intervals with velocity increasing as the depletion ratio increases. Here the dimension of y axis in (b) follows the symmetric logarithmic mode (e.g., `symlog` mode in `python` library `matplotlib`), with the threshold between log and linear scales set to 10^{-3}.

The comparative analysis between adsorption and partitioning charging reveals that these two mechanisms exhibit qualitatively similar but quantitatively different sensitivities to the oil depletion ratio, R_D. Under the adsorption charging model, the surface charge density σ_{ll} is prescribed as a constant; thus, the local electrostatic driving force at the interface remains invariant regardless of its spatial position. In contrast, for the partitioning charging case—characterized by a fixed potential difference $\Delta\varphi$—the results in Fig. 3 manifest a more pronounced nonlinear response to R_D. This discrepancy stems from the fundamental difference in electrostatic boundary conditions. In the partitioning model, the effective surface charge density is a conjugate quantity dictated by the local capacitance of the electric double layer. As the interface recedes into the groove, the proximity of the solid walls and the confinement of the electrolyte volume significantly alter the electrostatic screening environment. This geometric constraint modifies the local electric field gradient, resulting in a self-adjusting effective charge that renders the partitioning mechanism far more susceptible to recession depth than the constant-charge adsorption model.

Furthermore, the solid-liquid interface charge σ_{sl} acts as a critical modulator of the global flow field. When $\sigma_{sl} = -\sigma_0$ (opposing the interface charge), the system enters an antagonistic regime where the electroosmotic flows (EOF) generated at the wall and within the groove compete. The highlighted intervals in Fig. 3 denote regions where the slip velocity counterintuitively correlates positively with the depletion ratio. This phenomenon suggests that as R_D increases, the recessed configuration of the liquid-liquid interface shields its antagonistic flow from the main channel

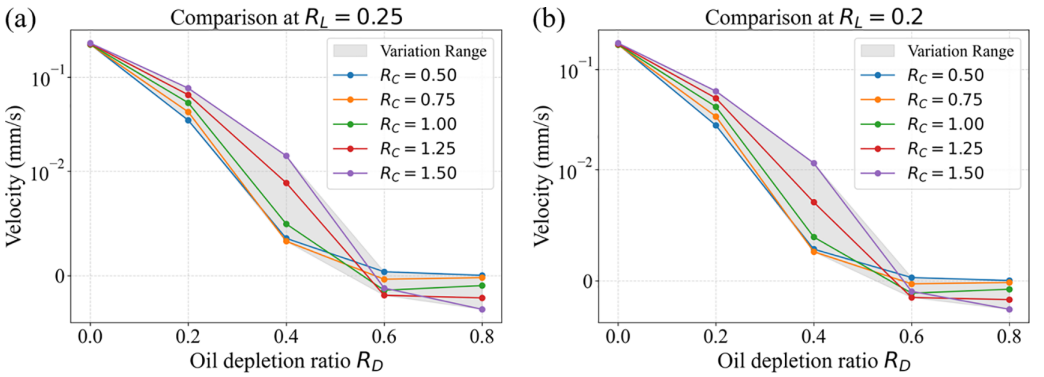

FIG. 4. Electroosmotic velocity versus oil depletion ratio for partitioning charging at the liquid-liquid interface in different geometric setups. Here the dimension of y axis follows the symmetric logarithmic mode, with the threshold between log and linear scales set to 10^{-2}. It is clearly shown that the variations of the resulting velocity between different cavity aspect ratios R_C are significant when the oil depletion ratio R_D lies in the interval abount 0.2 to 0.4, while the total velocity difference between the oil depletion ratio of $R_D = 0.0$ and $R_D = 0.8$ is slightly monotonically increasing as the cavity aspect ratio R_C varies.

more effectively than it attenuates the primary driving force. This subtle shift in the balance between opposing driving sites optimizes net momentum transfer to the bulk fluid. Consequently, the transition from monotonic to nonmonotonic velocity profiles underscores that the liquid depletion effect functions as a "spatial filter," reweighting the relative contributions of disparate charged surfaces to the global electroosmotic slip.

C. Geometric effect: Cavity aspect ratio and length

We further compare the electroosmotic slip velocities induced by partitioning charging under different geometric configurations, where the length-related geometric dimensionless parameters here are set to $R_C = 0.5, 0.75, 1, 1.25, 1.5$ and $R_L = 0.25, 0.2$, with $N = 2$. The liquid-liquid interface is assumed to be partitioning-charged with $\Delta\varphi = \varphi_T$ with $\sigma_{\mathrm{ll}} = \sigma_{\mathrm{sl}} = 0$. The results are shown in Fig. 4.

The parametric study presented in Fig. 4 focuses on the partitioning-charged interface to delineate how the cavity aspect ratio, R_C, governs the efficiency of the electroosmotic slip, while the cavity length R_L only shows quantitative effects with insignificant impact on the R_C-dependence. A pivotal observation is the marked divergence in velocity results when the depletion ratio, R_D, falls within the interval of 0.2 to 0.4. Within this transitional regime, the liquid-liquid interface resides near the "throat" of the groove, where the transition from the constrained cavity environment to the bulk flow is most abrupt. Minor variations in R_C induce significant alterations in the interfacial curvature and the effective hydraulic diameter. Specifically, for higher R_C, the widened cavity accommodates a more expansive recirculation zone. Depending on the precise location of the vortex core, this configuration can either facilitate momentum coupling to the main channel or promote enhanced energy dissipation, thereby driving the substantial velocity fluctuations observed as the flow field undergoes topological reconfiguration.

Beyond this transitional regime ($R_D > 0.6$), the influence of R_C on the global velocity magnitude becomes increasingly dominant. Data demonstrate that the velocity differential between the fully infused state ($R_D = 0$) and the highly depleted state ($R_D = 0.8$) scales monotonically with the cavity aspect ratio. This behavior suggests that in wider grooves (higher R_C), the shielding effect of the cavity is significantly intensified; as the oil phase depletes, the charged interface is buried deeper within an enlarged reservoir of stagnant or recirculating fluid. This spatial sequestration forces the induced EOF to dissipate more rigorously through viscous friction against the sidewalls before

its momentum can be imparted to the stress-free region of the main channel. Consequently, R_C emerges as a critical design parameter for SLIS-based microfluidic architectures. While a larger R_C offers an expanded range of velocity tunability, it concurrently renders the electroosmotic slip more susceptible to fluctuations in lubricant depletion, necessitating a careful balance between controllability and operational stability.

IV. ION PARTITION EFFECT ON STREAMING POTENTIAL

To investigate the aforementioned two-sided charge polarization coupling effect, this study focuses on the two-phase streaming potential effect of SLIS, with the system configuration shown in Fig. 1(b). For the liquid-liquid interface charging caused by ion partitioning, the diffuse layers on both sides carry opposite charges, resulting in inherent two-sided coupling. Specifically, under the same convective velocity conditions, this induces streaming potentials of opposite signs, which in turn lead to nonuniform distributions of the potential and diffuse layer charge densities on both sides. To highlight the possible streaming potential effect within the groove, a groove structure with dimensions $H_{\mathrm{cav}} \times L_{\mathrm{cav}}$ of 0.2×0.05 $\mu\mathrm{m}^2$ are selected, while the dimensions of the main channel $W_{\mathrm{main},1/2} \times L_{\mathrm{main}}$ are is $0.4 \times 0.2\,\mu\mathrm{m}$ with $N = 1$. The same ion concentrations in both phases are chosen, resulting in $\lambda_{\mathrm{D}} = 0.01\,\mu\mathrm{m}$, which is smaller than the groove depth of the system. The solid-liquid interface is uncharged, and the liquid-liquid interface is partitioning-charged with a distributed potential of $\Delta\varphi_\infty = -0.5V_T$. A pressure difference of $\Delta p \equiv p_{\mathrm{out}} - p_{\mathrm{in}} = 5\,\mathrm{kPa}$ is applied at the inlet and outlet boundaries, with both potential and velocity subjected to periodic conditions. The total simulation time is 1×10^{-5} s, by which the system has reached a steady state, and the typical results for the velocity and potential distributions are shown in Fig. 5.

As shown in Fig. 5(a), the pressure-driven flow in the main channel acts as a typical plate-driven flow for the fluid within the groove, exhibiting a characteristic vortex structure. At half the depth of the groove, the flow direction is opposite to that of the main channel [as illustrated in Fig. 5(c)]. For the potential field induced by the flow of the charged liquid-liquid interface, the distributions of the potential and electric field lines are shown in Fig. 5(b). In the main channel, cations near the liquid-liquid interface are transported downstream under the influence of convection and eventually accumulate near the downstream three-phase contact line, resulting in the periodic potential distribution at a quarter-width of the channel, as depicted in Fig. 5(d). This distribution arises because, after the establishment of the streaming potential in the main channel, internal closed circuits can form through the electrolyte solution along both the flow and counterflow directions, ultimately generating a streaming potential of approximately 0.15 mV. In contrast to the main channel, as shown in Fig. 5(c), the streaming potential within the groove is around 0.35 mV.

Here, we briefly analyze the possible reasons for the observed phenomena. If we consider the mechanism of convective transport of anions along the inner interface, the streaming potential between the upstream and downstream regions should theoretically be negative. However, since the groove is a closed structure, the net flow along the streamwise direction is zero. This leads to the mixing of anions between the upstream and downstream regions within the groove, thereby reducing the streaming potential effect caused by convection. Additionally, due to the two-sided coupling of diffuse layer charging at the liquid-liquid interface dominated by partitioning charging, while cations accumulate downstream in the main channel, anions within the groove also form a similar potential difference under the influence of the distributed potential, namely,

$$\begin{aligned}\varphi_{\mathrm{int,down}} - \varphi_{\mathrm{int,up}} &= (\varphi_{\mathrm{int,down}} - \varphi_{\mathrm{ext,down}}) + (\varphi_{\mathrm{ext,down}} - \varphi_{\mathrm{ext,up}}) + (\varphi_{\mathrm{ext,up}} - \varphi_{\mathrm{int,up}}) \\ &= \Delta\varphi_\infty + (\varphi_{\mathrm{ext,down}} - \varphi_{\mathrm{ext,up}}) + (-\Delta\varphi_\infty) \\ &= \varphi_{\mathrm{ext,down}} - \varphi_{\mathrm{ext,up}}.\end{aligned} \tag{10}$$

It is evident that the above derivation relies on the maintenance of an electrochemical equilibrium near the liquid-liquid interface. When the partitioning charge density at the liquid-liquid interface

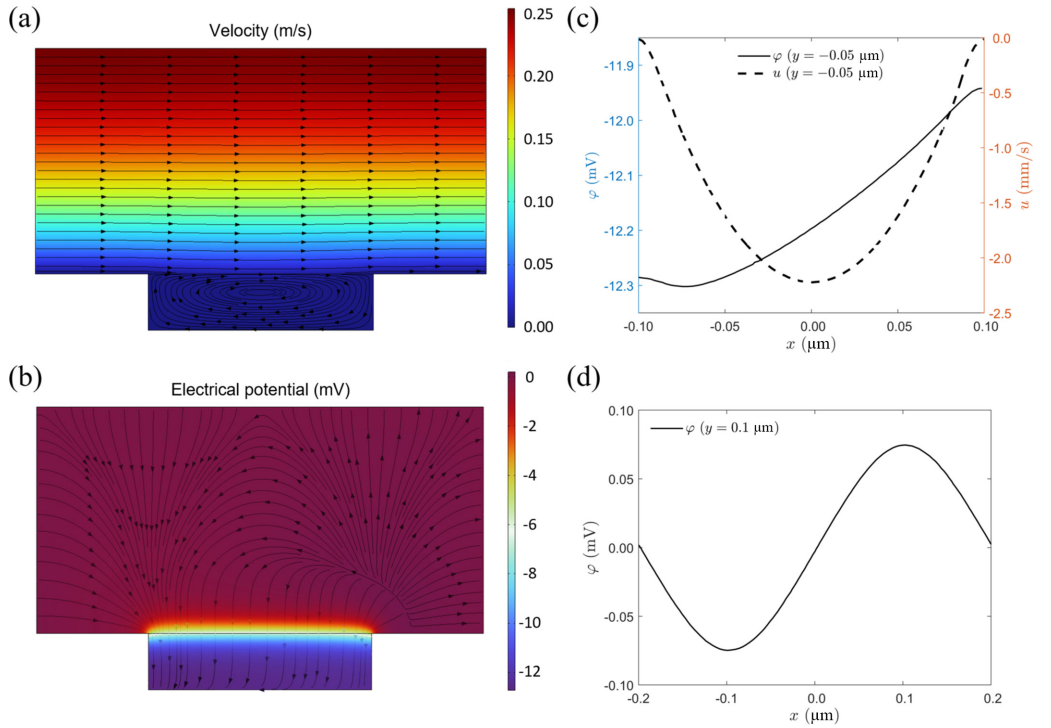

FIG. 5. Typical results of velocity and potential distributions for the streaming potential on liquid-immersed slip surfaces: Panels (a), (b) show the velocity field and potential field distributions, respectively; panels (c), (d) present the velocity and potential profile distributions in the groove region at $y = -0.05$ μm and in the main channel region at $y = 0.1$ μm, respectively.

is sufficiently large, this equilibrium may be disrupted, potentially leading to the formation of a characteristic diffusion boundary layer and surface conductance effects [5].

V. CONCLUSIONS

In this work, the direct numerical simulation based on the diffuse interface model is employed to investigate the electrokinetic transport mechanisms of SLIS, exploring the typical influencing mechanisms for electrokinetic regulation of multiphase flow at micro- and nanoscales. The effectiveness of the direct simulation approach in addressing the ion relaxation effects of interfacial charging processes is first validated using basic model systems such as two-phase parallel electroosmosis. Subsequently, for typical systems involving electroosmosis and streaming potential on SLIS, the mechanisms of groove liquid depletion effects and two-sided charging polarization coupling effects are examined. The study reveals the electroosmotic velocity reversal effect induced by geometric configurations and the two-sided streaming potential effect induced by mixing and partitioning charging.

Our findings provide foundational insights and inspiration for the rational design of quantitative regulation schemes for multiphase flow and transport at micro- and nanoscales. Future research directions may include: (1) further exploration of the effects of complex geometries and surface properties on electrokinetic transport in SLIS; (2) investigation of the interplay between electrokinetic phenomena and other physical processes, such as thermal effects and chemical reactions; and (3) experimental validation of the simulation results to enhance the practical applicability of the findings.

ACKNOWLEDGMENTS

This work was financially supported by the National Natural Science Foundation of China (Grants No. 12432013 and No. 12272207). The authors thank the anonymous referee who provided useful and detailed comments on the manuscript.

DATA AVAILABILITY

The data that support the findings of this article are openly available [44].

APPENDIX: VERIFICATION OF DIRECT NUMERICAL SIMULATION APPROACH

Due to the lack of standard test cases for complex electrokinetic transport at liquid-liquid interfaces, a typical degenerate scenario will be selected here to verify the solver, and the main challenges currently faced along with potential solutions will be briefly discussed. As a degenerate scenario under electrochemical quasiequilibrium conditions, the two-phase parallel electroosmotic system studied in previous work is chosen as the model system [7]. To verify the direct numerical solution scheme for the electrostatic Poisson equation, the modified Nernst-Planck equation, and the Cahn-Hilliard-Navier-Stokes equation system, the results will be compared and validated against those obtained using the regular perturbation method.

For simplicity, only the case of a liquid-liquid interface with partition-induced charges is considered here. The solution concentrations in both the oil and water phases are $c_\infty = 1\,\mathrm{mM}$, and the equilibrium distribution potential is $\Delta\varphi_\infty = -2V_T$, where $V_T \equiv k_\mathrm{B}T/e$. The half-width of the microchannel is $0.5\,\mu\mathrm{m}$, resulting in a characteristic thickness of the electric double layer of $\lambda_\mathrm{D} \simeq 10\,\mathrm{nm}$, allowing the overlapping effect of the electric double layers to be neglected. The length of the simulated channel segment is $L = 5\,\mu\mathrm{m}$, and the applied electric field strength is $E_\infty = 10^5\ \mathrm{V/m}$. Consequently, the potential difference at the inlet and outlet boundaries of phase α is $\varphi_{\mathrm{out},\alpha} - \varphi_{\mathrm{in},\alpha} = E_\infty L = 0.5\,\mathrm{V}$. Periodic boundary conditions are applied to the velocity, pressure, and concentration fields (with $\Delta p = 0$).

In real oil-water interface systems, a distributed potential exists between the electrically neutral regions on both sides of the interface, i.e.,

$$\varphi_{\mathrm{out},2} - \varphi_{\mathrm{out},1} = \varphi_{\mathrm{in},2} - \varphi_{\mathrm{in},1} = \Delta\varphi_\infty. \tag{A1}$$

In principle, the interfacial potential distribution at the inlet and outlet should also satisfy the electrochemical quasiequilibrium state. However, in numerical solutions, imposing the latter boundary condition is not straightforward. Therefore, here, a uniform potential is applied at the inlet and outlet,

$$\varphi_\mathrm{in} = \mathrm{const}, \quad \varphi_\mathrm{out} = \mathrm{const} + E_\infty L, \tag{A2}$$

or a stepwise interfacial potential distribution is imposed,

$$\varphi_\mathrm{in}(\phi) = \Delta\varphi_\infty \mathcal{H}(\phi), \quad \varphi_\mathrm{out} = \Delta\varphi_\infty \mathcal{H}(\phi) + E_\infty L, \tag{A3}$$

where the total channel length is long enough to provide a buffer zone for inlet and outlet effects. In practice, the above inlet and outlet conditions correspond to oil-water interface two-liquid parallel electroosmotic systems with screen printing electrodes upstream and downstream, with or without baffles at the oil-water interface. Simulation results have shown that the total length of 5 μm selected for this study is sufficient to eliminate the nonequilibrium potential effects at the inlet and outlet.

In Figs. 6 and 7, panels (a) and (b) respectively present the steady-state results of the potential field and velocity field distributions from the direct numerical simulation validation of the two-liquid parallel electroosmotic flow. The inlet and outlet effects are clearly observable in the velocity field distribution when a uniform potential is applied at the inlet and outlet boundaries. Figures 6(c) and 7(c) show the evolution of the potential field and velocity field profiles under the stepwise potential boundary condition, demonstrating that they eventually converge to the regular perturbation

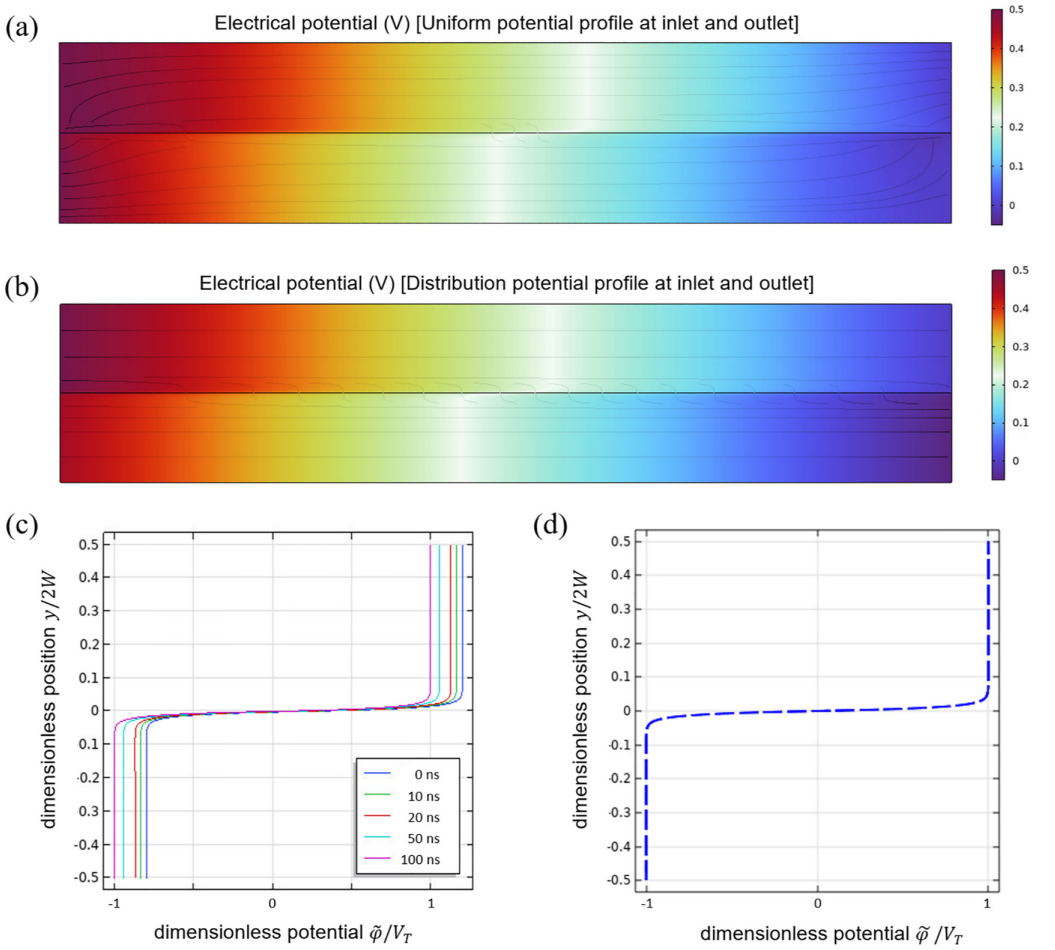

FIG. 6. Verification of direct numerical simulation for two-phase parallel electroosmotic flow: evolution of the potential field distribution. Panels (a), (b) show the steady-state distributions of the potential field when the interfacial potential jump at the boundary is zero and distributed, respectively. Panels (c), (d) present a comparison between the evolution of the potential field distribution from direct numerical simulation and the results based on the regular perturbation solution.

solution depicted in Figs. 6(d) and 7(d). This validates that the direct numerical simulation of the diffuse interface model can accurately reproduce the degenerate scenario under electrochemical quasiequilibrium conditions.

It is noteworthy that, compared with the electrophoresis of charged droplets described using the sharp interface model, direct numerical simulations based on the diffuse interface model still present significant challenges. In fact, even without considering the scenario of spontaneous charge distribution, merely accounting for spontaneous adsorption charging at liquid-liquid multiphase soft interfaces and the associated nonequilibrium transport behaviors poses substantial difficulties in numerical simulations using the diffuse interface model, particularly in adapting the computational domain to practical large-scale requirements. For instance, unlike weakly conductive dielectrics with thicker diffuse layers often used in electrohydrodynamic systems, systems like droplet electrophoresis, which feature thinner diffuse layers, may see the finite thickness of the solvent mixing layer play a crucial role, significantly increasing the cost of adaptive mesh refinement. This has

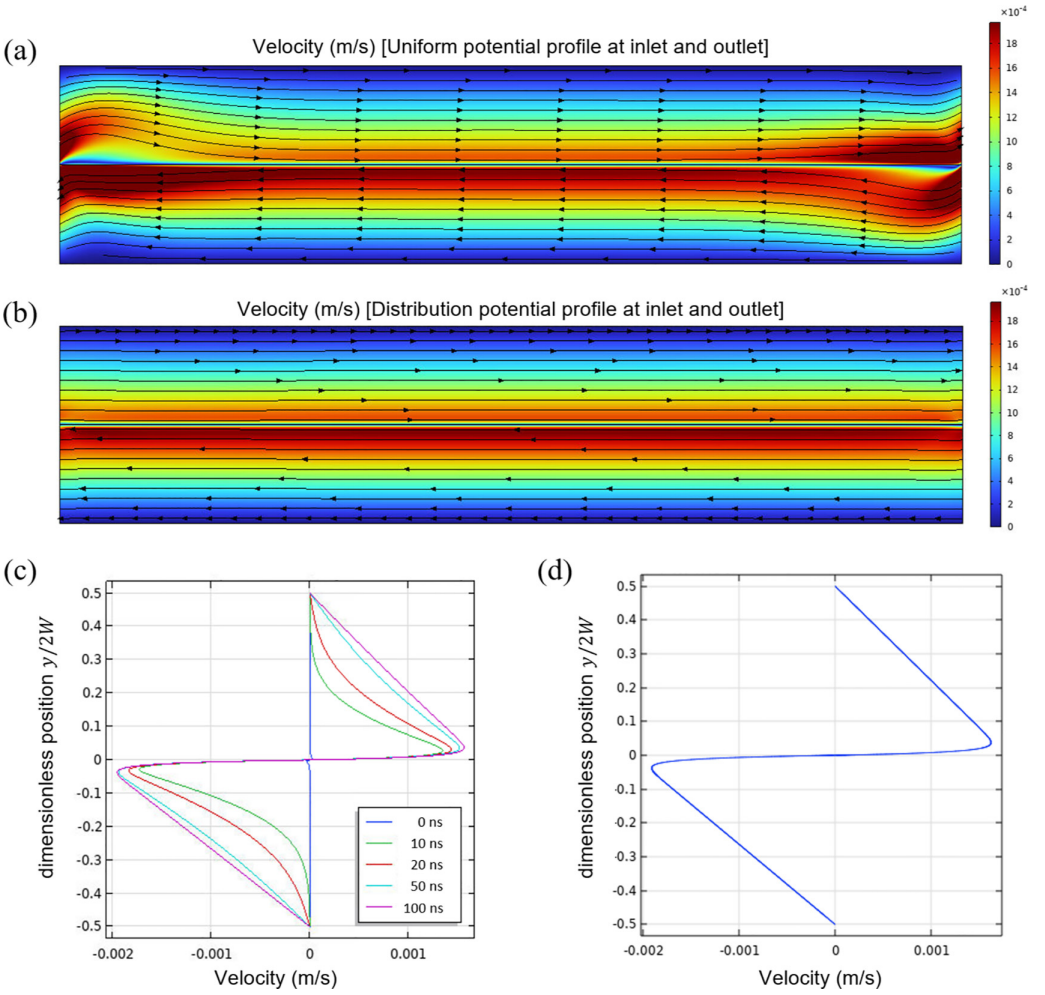

FIG. 7. Verification of direct numerical simulation for two-phase parallel electroosmotic flow: evolution of the velocity field distribution. Panels (a), (b) show the steady-state distributions of the velocity field when the interfacial potential jump at the boundary is zero and distributed, respectively. Panels (c), (d) present a comparison between the evolution of the velocity profile distribution from direct numerical simulation and the results based on the regular perturbation solution.

confined existing numerical simulation studies either to small-scale systems [38] or to potentially questionable interface resolution accuracy [45,46]. In contrast, numerical solutions for droplet electrophoresis using the sharp interface model are more common, but these typically achieve quantitative solutions only under fixed interface shapes, and previous studies have often failed to effectively capture the influence of the solvent mixing layer. The impact of the solvent mixing layer can be addressed through the mesoscopic model-based interface condition corrections discussed earlier [7]; alternatively, using effective interface conditions derived from asymptotic expansions can also provide quantitative results for minor shape changes at the interface [39].

[1] K. G. Marinova, R. G. Alargova, N. D. Denkov, O. D. Velev, D. N. Petsev, I. B. Ivanov, and R. P. Borwankar, Charging of oil-water interfaces due to spontaneous adsorption of hydroxyl ions, Langmuir **12**, 2045 (1996).
[2] A. G. Volkov, D. W. Deamer, D. L. Tanelian, and V. S. Markin, Electrical double layers at the oil/water interface, Prog. Surf. Sci. **53**, 1 (1996).
[3] T. M. Squires and S. R. Quake, Microfluidics: Fluid physics at the nanoliter scale, Rev. Mod. Phys. **77**, 977 (2005).
[4] Y. Huang and M. Wang, Electrokinetic multiphase hydrodynamics, Appl. Phys. Rev. **12**, 031322 (2025).
[5] A. J. Pascall and T. M. Squires, Electrokinetics at liquid/liquid interfaces, J. Fluid Mech. **684**, 163 (2011).
[6] F. Yang, S. Shin, and H. A. Stone, Diffusiophoresis of a charged drop, J. Fluid Mech. **852**, 37 (2018).
[7] Y. Huang and M. Wang, Solvent mixing and ion partitioning effects in spontaneous charging and electrokinetic flow of immiscible liquid-liquid interface, Phys. Rev. Fluids **9**, 103701 (2024).
[8] H. A. Stone, A. D. Stroock, and A. Ajdari, Engineering flows in small devices: Microfluidics toward a lab-on-a-chip, Annu. Rev. Fluid Mech. **36**, 381 (2004).
[9] M. Mirzadeh and M. Z. Bazant, Electrokinetic control of viscous fingering, Phys. Rev. Lett. **119**, 174501 (2017).
[10] D. Lohse, Bubble puzzles: From fundamentals to applications, Phys. Rev. Fluids **3**, 110504 (2018).
[11] P. M. Vlahovska, Electrohydrodynamics of drops and vesicles, Annu. Rev. Fluid Mech. **51**, 305 (2019).
[12] Y. Huang and M. Wang, Electrokinetics at liquid-liquid interfaces: Physical models and transport mechanisms, Adv. Colloid Interface Sci. **342**, 103518 (2025).
[13] S. Dehe, B. Rofman, M. Bercovici, and S. Hardt, Electro-osmotic flow enhancement over superhydrophobic surfaces, Phys. Rev. Fluids **5**, 053701 (2020).
[14] L. N. Carenza, L. Biferale, and G. Gonnella, Multiscale control of active emulsion dynamics, Phys. Rev. Fluids **5**, 011302(R) (2020).
[15] X. Pan, M. Hu, B. Xu, F. Wang, P. Huo, F. Chen, Z. Gu, and D. Deng, Armstrong liquid bridge: Formation, evolution and breakup, Phys. Rev. Fluids **6**, 093901 (2021).
[16] D. S. Pillai, K. C. Sahu, and R. Narayanan, Electrowetting of a leaky dielectric droplet under a time-periodic electric field, Phys. Rev. Fluids **6**, 073701 (2021).
[17] E. Karimi-Sibaki, A. Vakhrushev, A. Kadylnykova, M. Wu, A. Ludwig, J. Bohacek, and A. Kharicha, A multiphase model for exploring electrochemical Marangoni flow, Electrochem. Comm. **155**, 107567 (2023).
[18] A. Dubey, G. P. Bewley, K. Gustavsson, and B. Mehlig, Critical charges for droplet collisions, Phys. Rev. Fluids **9**, 074302 (2024).
[19] A. Bandopadhyay, S. Mandal, and S. Chakraborty, Streaming potential-modulated capillary filling dynamics of immiscible fluids, Soft Matter **12**, 2056 (2016).
[20] J. Maes and S. Geiger, Direct pore-scale reactive transport modelling of dynamic wettability changes induced by surface complexation, Adv. Water Resour. **111**, 6 (2018).
[21] M. O. Abu-Al-Saud, S. Esmaeilzadeh, A. Riaz, and H. A. Tchelepi, Pore-scale study of water salinity effect on thin-film stability for a moving oil droplet, J. Colloid Interface Sci. **569**, 366 (2020).
[22] S. Dehe, M. Hartmann, A. Bandopadhyay, and S. Hardt, Controlling the electrostatic Faraday instability using superposed electric fields, Phys. Rev. Fluids **7**, L082002 (2022).
[23] S. Dehe, M. Hartmann, A. Bandopadhyay, and S. Hardt, The spatial structure of electrostatically forced Faraday waves, J. Fluid Mech. **939**, A6 (2022).
[24] A. Alizadeh, Y. Huang, F. Liu, H. Daiguji, and M. Wang, A streaming-potential-based microfluidic measurement of surface charge at immiscible liquid-liquid interface, Int. J. Mech. Sci. **247**, 108200 (2023).
[25] S. Hardt and G. McHale, Flow and drop transport along liquid-infused surfaces, Annu. Rev. Fluid Mech. **54**, 83 (2022).
[26] T.-S. Wong, S. H. Kang, S. K. Y. Tang, E. J. Smythe, B. D. Hatton, A. Grinthal, and J. Aizenberg, Bioinspired self-repairing slippery surfaces with pressure-stable omniphobicity, Nature (London) **477**, 443 (2011).

[27] S. Wang, X. Yang, F. Wu, L. Min, X. Chen, and X. Hou, Inner surface design of functional microchannels for microscale flow control, Small **16**, 1905318 (2020).
[28] E. Lauga and H. A. Stone, Effective slip in pressure-driven Stokes flow, J. Fluid Mech. **489**, 55 (2003).
[29] J. P. Rothstein, Slip on superhydrophobic surfaces, Annu. Rev. Fluid Mech. **42**, 89 (2010).
[30] T. M. Squires, Electrokinetic flows over inhomogeneously slipping surfaces, Phys. Fluids **20**, 092105 (2008).
[31] S. S. Bahga, O. I. Vinogradova, and M. Z. Bazant, Anisotropic electro-osmotic flow over superhydrophobic surfaces, J. Fluid Mech. **644**, 245 (2010).
[32] A. V. Belyaev and O. I. Vinogradova, Electro-osmosis on anisotropic superhydrophobic surfaces, Phys. Rev. Lett. **107**, 098301 (2011).
[33] J. S. Wexler, I. Jacobi, and H. A. Stone, Shear-driven failure of liquid-infused surfaces, Phys. Rev. Lett. **114**, 168301 (2015).
[34] C. Vega-Sánchez and C. Neto, Slightly depleted lubricant-infused surfaces are no longer slippery, Langmuir **38**, 10568 (2022).
[35] B. Fan, A. Bhattacharya, and P. R. Bandaru, Enhanced voltage generation through electrolyte flow on liquid-filled surfaces, Nat. Commun. **9**, 4050 (2018).
[36] B. Fan and P. R. Bandaru, Modulation of the streaming potential and slip characteristics in electrolyte flow over liquid-filled surfaces, Langmuir **35**, 6203 (2019).
[37] B. Fan and P. R. Bandaru, Tensorial modulation of electrokinetic streaming potentials on air and liquid filled surfaces, Langmuir **35**, 14812 (2019).
[38] B. Rotenberg, I. Pagonabarraga, and D. Frenkel, Coarse-grained simulations of charge, current and flow in heterogeneous media, Faraday Discuss. **144**, 223 (2010).
[39] O. Schnitzer, I. Frankel, and E. Yariv, Electrokinetic flows about conducting drops, J. Fluid Mech. **722**, 394 (2013).
[40] D. Jacqmin, Contact-line dynamics of a diffuse fluid interface, J. Fluid Mech. **402**, 57 (2000).
[41] F. Liu and M. Wang, Wettability effects on mobilization of ganglia during displacement, Int. J. Mech. Sci. **215**, 106933 (2022).
[42] F. Liu and M. Wang, Phase diagram for preferential flow in dual permeable media, J. Fluid Mech. **948**, A19 (2022).
[43] R. A. W. Dryfe, The electrified liquid-liquid interface, Adv. Chem. Phys. **141**, 153 (2009).
[44] Y. Huang and M. Wang, Simulation result of electrokinetic transport regulation at liquid-infused surface [Data set], Zenodo, 2026, https://doi.org/10.5281/zenodo.20382097.
[45] O. Shardt, S. K. Mitra, and J. J. Derksen, Simulations of charged droplet collisions in shear flow, Chem. Eng. J. **302**, 314 (2016).
[46] N. Rivas, S. Frijters, I. Pagonabarraga, and J. Harting, Mesoscopic electrohydrodynamic simulations of binary colloidal suspensions, J. Chem. Phys. **148**, 144101 (2018).